



Tungsten as an interface agent leading to highly active and stable copper–ceria water gas shift catalyst

Anna Kubacka^a, Rui Si^b, Piotr Michorczyk^{a,c}, Arturo Martínez-Arias^a, Wenqian Xu^b, Jonathan C. Hanson^b, José A. Rodríguez^{b,*}, Marcos Fernández-García^{a,**}

^a Instituto de Catálisis y Petroleoquímica, CSIC, Campus Cantoblanco, 28049 Madrid, Spain

^b Chemistry Department, Brookhaven National Laboratory, Upton, NY 11973, USA

^c Institute of Organic Chemistry and Technology, Cracow University of Technology, Warszawska 24, 31-155 Kraków, Poland

ARTICLE INFO

Article history:

Received 25 September 2012

Received in revised form 7 December 2012

Accepted 10 December 2012

Available online 20 December 2012

Keywords:

WGS catalyst

Mixed oxides

Ceria

Copper

Tungsten

In situ XRD

XAFS

Vibrational

ABSTRACT

A series of W–Cu–Ce mixed oxide catalysts prepared by microemulsion was evaluated in the water–gas shift (WGS) reaction. At low temperatures (<350 °C), the total conversion of CO on the W–Cu–Ce systems was two times larger than on binary Cu–Ce mixed oxides which are well known catalysts for the WGS. In addition and in contrast with Cu–Ce, W–Cu–Ce catalysts were stable and no signs of deactivation were found after 10 h of reaction time. The rationale for the excellent catalytic performance presented by the W–Cu–Ce ternary oxide was elucidated from the viewpoint of a complete structural (e.g. analysis of the long and short range order) and redox behavior characterization using in situ, time-resolved X-ray diffraction (XRD) as well as X-ray absorption (XAS), infrared (diffuse reflectance Fourier transform DRIFTS) and Raman spectroscopies. From a single phase fluorite-type structure, the catalysts show significant structure/redox evolution under reaction conditions as a function of the W and Cu content. As it occurs in the parent Cu–Ce system, the dominant presence of metallic Cu and fluorite-type oxide phases is detected under reaction conditions for the ternary systems. An outstanding promotion of catalytic properties is nevertheless evidenced for samples with W content above 10 at.% and is shown to be related to the presence of oxidized W–Cu local entities. Such local entities, which are obviously characteristic of the ternary system, greatly enhance fluorite redox properties and play an interfacial role between the main metallic Cu and fluorite-type oxide phases. As a consequence of all these effects, incorporation of W into the initial material leads to efficient WGS catalysts, most promising for their application in the so-called low temperature region, e.g. below 350 °C.

© 2012 Elsevier B.V. All rights reserved.

1. Introduction

Challenges in energy and environmental fields call for the development of highly active and stable catalysts, allowing for more efficient and cleaner processes [1]. The water gas shift reaction (WGS; $\text{CO} + \text{H}_2\text{O} \rightleftharpoons \text{H}_2 + \text{CO}_2$) has become a leading technology in the chemical industry, particularly in relation to the production of clean hydrogen and energy recovering systems [2]. In this field, alternatives to Cu–ZnO based systems that may work with reasonable stability at low temperatures, e.g. below 350 °C are actively sought. Ceria-based materials have shown rather interesting properties in WGS during recent years, unveiling thus potential to become real alternatives in the future [2,3].

Cu–CeO₂ systems are among the most active WGS systems and, compared with Pt, Pd, Au and, generally, expensive noble metal based materials, they constitute an interesting alternative from an economical point of view. Among possible different configurations of Cu–CeO₂ materials, Cu–Ce mixed oxides have shown reasonable activity and relatively good stability [4–6]. Due to the different chemical and usually structural properties of doping metals (such as Cu) at Ce-based oxide environments, doping of ceria strongly affects its inherent physico-chemical properties [7]. At a structural level, a dopant can introduce stress into the lattice of an oxide host, inducing in this way the formation of defects to fulfill charge neutrality and modifying chemical reactivity. On the other hand, the lattice of the oxide host can impose on the dopant element non-typical coordination modes with the subsequent perturbation in the dopant chemical properties. Furthermore, the combination of two metals in an oxide matrix can produce materials with novel structural or electronic properties derived either directly from the chemical state of the doping agent and/or by the corresponding charge neutrality defects that can lead to superior catalytic activity or selectivity [4,5,8–14].

* Corresponding author.

** Corresponding author. Tel.: +34 915 85 4943; fax: +34 915 85 47 60.

E-mail addresses: rodriguez@bnl.gov (J.A. Rodríguez), mfg@icp.csic.es, m.fernandez@icp.csic.es (M. Fernández-García).

As a general rule, the activity for WGS of systems containing reducible oxides as ceria and “active” species as copper is intimately related to the performance of the copper-ceria interface. Moreover, it appears that highly active ceria-based materials perform dominantly through a redox mechanism, being formate-related mechanisms only of relevance in cases where poor activity is observed [4,15,16]. Furthermore, the presence and capital role of ceria vacancies at copper-ceria interfaces (e.g., a Cu–O vacancy interaction) is well established while the exact Cu active species is more complex to be definitively settled down. The exact chemical state of the system appears however partially (e.g. Cu⁺) or totally reduced (Cu⁰) [4–6,10–13,17]. Cu–CeO₂ seems in any case a rather unique system to define the copper oxidation state as Cu appears to be (partially) reversibly in and out of the fluorite structure in response to the oxidizing or reducing nature of the gas atmosphere with a concomitant change in oxidation state. This behavior has been only observed up to now for Cu and Pd (and possibly Pt) at the Ce-fluorite solid solutions [4,12b,18,19,20]. In any case, this quasi-free state of copper may explain the difficulty in getting a definitive assignment of the Cu active species in several chemical reactions like CO oxidation, CO preferential oxidation, water gas shift, etc.

The quest of improving chemical activity of Cu–Ce requires the development of novel, advanced materials. In this work we investigate the effect of tungsten introduction on a Cu–Ce mixed oxide matrix for the WGS reaction upon formation of a ternary mixed oxide. Our findings indicate that the rich chemistry of Cu in a ceria matrix and its inherent potential in the WGS reaction through Cu–Ce interfaces [3–6,10–14,21] can be modulated by the presence of a third species, in this case W. We will show here that tungsten addition to the catalyst formulation renders a highly active and stable catalyst, particularly in the low temperature region, below 350 °C. To this end, an in situ study of the W–Cu–Ce system behavior under WGS was carried out with the help of synchrotron-based X-ray diffraction (XRD) and absorption (XAS) techniques, complemented with vibrational infrared and Raman spectroscopic tools. The analysis indicates that W affects both the cerium and the copper components but key elements are related to the formation of W–Cu local entities which definitively modulate the redox behavior of the ceria phase in reaction conditions.

2. Experimental

2.1. Sample preparation

The W–Cu–Ce catalysts were prepared by employing reverse microemulsions containing n-Heptane, Triton-X-100 and n-Hexanol as organic solvent, surfactant and cosurfactant, respectively, in amounts similar to those reported previously [4,22]. The required amount of ceria nitrate (Aldrich) copper nitrate (Aldrich) and ammonium tungsten oxide (Aldrich) was dissolved in distilled water and dispersed within already mentioned organic components to form the reverse microemulsion. Simultaneously, another microemulsion of similar characteristics was prepared containing dissolved in its aqueous phase the required amount of tetramethyl ammonium hydroxide (TMAH). After 1 h stirring of the two microemulsions, the TMAH-containing one was added to the metal-containing one and it was left for the period of 18–24 h in order to complete the precipitation reaction. The resulting solid was then separated by centrifugation and decantation, rinsed with methanol, dried overnight at 100 °C and the resulting powder was calcined at 500 °C for 2 h under air. Similar reference Cu–Ce, W–Ce and Ce systems were obtained by the same method. Chemical compositions were analyzed by ICP-AES and correspond to the ones mentioned in samples names in Table S1 (supporting information)

within a maximum error of ± 2 at.%. Table S1 also displays the BET specific surface areas of the materials.

2.2. Catalytic measurements

The catalysts were tested in a quartz tubular catalytic reactor for their activity under an atmospheric pressure flow (using mass flow controllers to prepare the reactant mixture except for water which was injected in a warm line using a syringe pump) of 3% CO, 3% H₂O (Ar balance), with a total flow of ca. 100 mL min^{−1} (roughly corresponding to 42,000 h^{−1} GHSV). Catalytic runs were followed using a mass spectrometer (Pfeiffer Omnistar 300) and Gas Chromatography (GC-2014 Shimadzu). Tests were carried out in the 200–450 °C interval at 50 °C steps, maintaining the reaction temperature at each plateau up to quasi-steady state equilibrium (typically 30–60 min). Additional tests were used to ensure the absence of methanation, CO preferential oxidation, or other possible side reactions. This was checked by the exclusive presence of H₂ and CO₂ products in the correct stoichiometric quantities. Finally, stability isothermal tests were run at 300 °C.

2.3. X-ray diffraction

In situ time-resolved X-ray diffraction (TR-XRD) experiments were carried out on beam line X7B of the National Synchrotron Light Source (NSLS) at Brookhaven National Laboratory (BNL) using an excitation energy of ~ 38.8 KeV ($\lambda = 0.3196$ Å). The sample (~ 5 mg) was loaded into a glass or quartz reactor of 1 mm diameter, which was attached to a flow system [23,24]. A small resistance heater was wrapped around the capillary, and the temperature was monitored with a 0.5 mm chromel–alumel thermocouple placed in the capillary near the sample. Two-dimensional powder patterns were collected with a Perkin-Elmer image plate detector and the powder diffraction rings were integrated using the FIT2D code [25]. The instrument parameters (Thompson-Cox-Hastings profile coefficients) were derived from the fit of a LaB₆ reference pattern. Rietveld profile refinements were performed with the aid of GSAS software [26,27]. The series of powder patterns were refined by sequential analysis where the starting model is based on the earlier powder pattern. Diffraction patterns were collected over the catalyst during the WGS reaction or several specific atmospheres containing H₂O or CO. Similarly to the catalytic test, the WGS reaction was carried out with a stepped temperature program from room temperature to 400 °C, with 2 h soaks at every 100 °C beyond 200 °C amid a 3% CO, 3% H₂O (He balance) gas mixture flow rate of 10 mL min^{−1} at a space velocity of 42,000 h^{−1}. Additional isothermal experiments were carried out at 300 °C by subjecting the sample to different atmospheres and obtaining quasi-equilibrium states.

2.4. XAFS

Cu K-edge and W L₃-edge in situ near-edge (XANES) and extended (EXAFS) absorption fine structure spectra were collected at beamline X18A and X19A of the NSLS at BNL under similar operational conditions as those for the catalytic and TR-XRD experiments. The same cell was used for the XAS experiments as that for in situ XRD, except that the sample was loaded into a Kapton tube (I.D. = 1/8 inch). The X-ray absorption spectra were taken repeatedly in the “fluorescence-yield mode” using a passivated implanted planar silicon (PIPS) detector cooled with circulating water. Due to the strong Ce-related fluorescence background, useful EXAFS data were only acquired at room temperature after maintaining the systems in WGS at 300 °C for 1 h and cooling down in the same testing atmosphere. The XANES and EXAFS data were then analyzed using the Athena [28,29] and VIPER (www.dessy.de/klmn/viper.html)

[30]) programs. Cu–O, Cu–Cu, W–O, W–Cu, and W–Ce reference phase functions for EXAFS analysis were obtained using the FEFF8.2 code [31]. The goodness of FEFF8.2 calculations for analyzing phase and amplitude functions was tested by simulating Cu and W foils as well as Cu_2O , CuO and monoclinic WO_3 experimental spectra. EXAFS error bars were estimated with k^1/k^2 weighted fittings.

2.5. Vibrational spectroscopies

IR spectra were performed using a Bruker Equinox 55 FTIR fitted with a MCT detector and a Harrick DRIFTS cell. Samples of ca. 50 mg were subjected to reaction conditions (as described above) from 200 °C to 450 °C at 50 °C steps in the WGS mixture used for catalytic experiments and in absence of CO gas. 70 spectra were recorded after each step ensuring that the measurements are carried out in stationary conditions both at the surface and at the gas phase (the latter verified by using a down stream on-line mass spectrometer described above). Raman spectra of fresh and used (in catalytic experiments at 300 °C during 1 h) samples were collected with an iHR320 Horiba Jobin-Yvon spectrometer equipped with a He:Ne laser (633 nm).

3. Results and discussion

The activity of the W–Cu–Ce catalysts during WGS is presented in Fig. 1. The plot shows that W–Ce and CeO_2 reference compounds present only marginal activity while the Cu–Ce reference compound is reasonably active. Note that the 20:80 at.% ratio selected for this compound renders the maximum activity presented among Cu–Ce mixed oxide catalysts previously reported [4]. The activity is however of moderate magnitude if compared with highly active copper-ceria systems [2,4,6,21,32]. Note on the other hand that in Cu– CeO_2 systems, activity and stability frequently showed opposite trends [21,33].

Addition of W to the mixed oxide already proved modestly positive from the initial concentration tested, 5 at.%, being in this case effective at temperatures above 250 °C. Higher quantities of W render better results and the two additional formulations tested display enhanced activity already from 200 °C. This is particularly true when we calculated normalized rates per surface Cu entity (see supporting information Fig. S1). The best catalyst corresponds to the W20Cu20Ce60 system, which reaches the conversion value corresponding to the thermodynamic equilibrium around 300 °C. This corresponds to a highly active system if compared with typical copper-ceria materials [2,4,6,21,33]. Moreover, the system is also stable working at a spatial velocity above $40,000 \text{ h}^{-1}$. Fig. 1 (bottom panel) provides evidence in this respect under conditions where Cu20Ce80 (and many other including Cu–ZnO based systems) catalyst(s) displays appreciable deactivation with time on stream [2,4,6,21,33]. Both capabilities high activity and stability are only observed for very few catalysts, mainly based in noble metals highly stabilized by strong interaction with the ceria support [2]. Of course, such materials are expensive and thus require alternative systems for future developments.

The apparent energy of activation of the reaction was calculated using the low temperature range of measurements; e.g. 473–573 K. This observable varies from 27.5 kJ mol^{-1} to 22.5 kJ mol^{-1} in going from Cu20Ce80 to W20Cu20Ce60 samples. First to say is that such low energy of activation values indicate the potential usefulness of the system for the low temperature region. Also, differences among catalysts would point out differences in the nature of the active center, which will be further characterized here using physico-chemical techniques [2,34]. Both points are further discussed below.

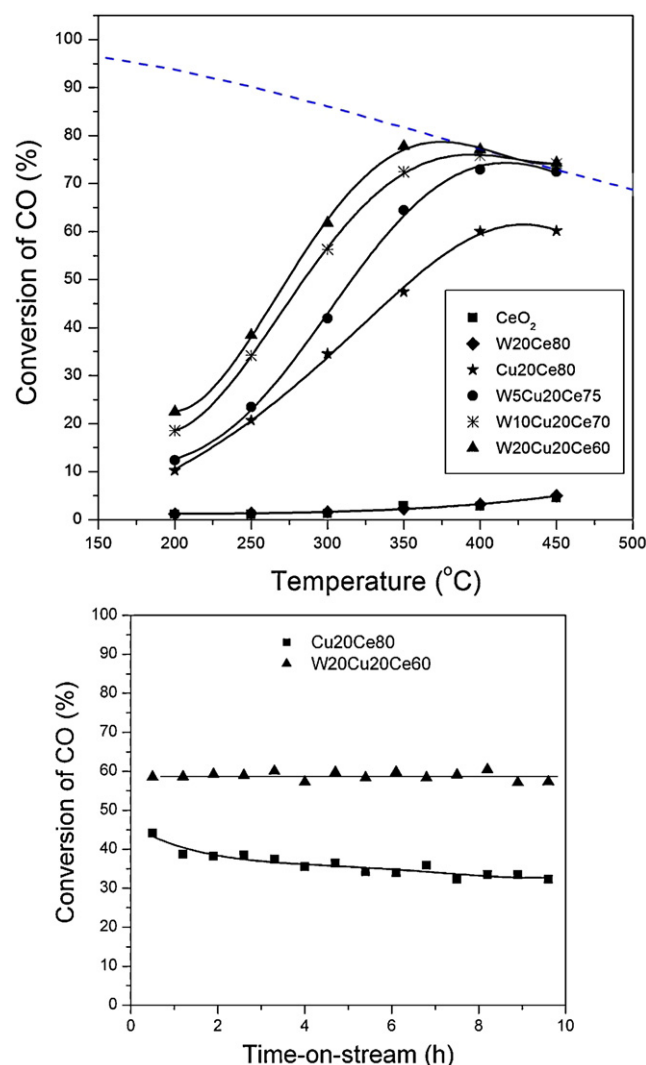


Fig. 1. Upper panel: CO conversion as a function of temperature for W–Cu–Ce samples and reference materials. The blue dotted line plots maximum CO conversion values corresponding to gas phase equilibrium under employed conditions. Lower panel: Catalytic stability test under WGS conditions at 300 °C for W20Cu20Ce80 and Cu20Ce80 samples. (For interpretation of the references to color in the artwork, the reader is referred to the web version of the article.)

In order to understand the physical basis of the outstanding catalytic behavior of W–Cu–Ce materials, an *operando* study of the systems was carried out. Concerning XRD results, Fig. 2 displays selected data while Fig. 3 presents the fluorite cell parameter obtained from Rietveld analysis. Fig. 2 shows that initially all samples (Cu–Ce and W–Ce reference as well as W–Cu–Ce ternary systems) present dominant fluorite-type reflections [35]. Only in the W5Cu20Ce75 and W20Cu20Ce60 cases we observed weak contributions attributable to, respectively, reduced [36] and CuO [37] species. Under a WGS atmosphere, already at the initial temperature tested (200 °C) we can only observe the presence of metallic fcc copper for all W–Cu–Ce samples as well as for the Cu–Ce reference. Such Cu phase is relatively similar in all cases although it appears to have a larger particle size for the W20Cu20Ce60 sample. This is further analyzed with the help of XAS. No W-single phase is observed.

Fig. 3 plots the Rietveld results corresponding to the fluorite cell parameter evolution under the WGS reaction conditions. The ternary W–Cu–Ce mixed oxides present a strong and gradual increase of the fluorite cell parameter which is a combination

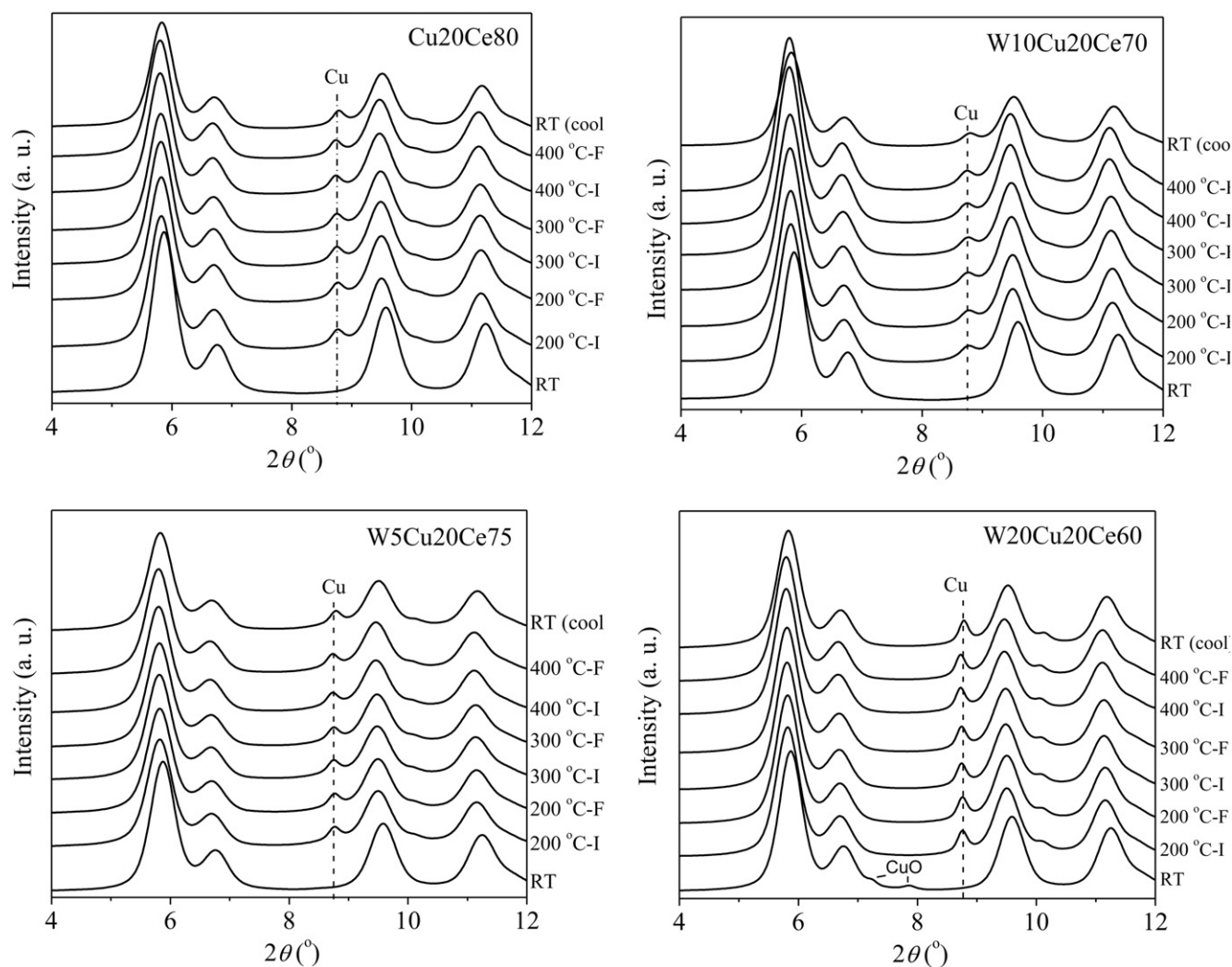


Fig. 2. Time resolved diffraction patterns of W–Cu–Ce and Cu–Ce samples during a WGS temperature ramp. Only selected diffractograms at initial (–I) and final (–F) points of indicated isothermal steps are presented (see text for details).

of a series of phenomena including a (small) thermal effect, the elimination (according to Fig. 2) of Cu from cationic positions of the structure (through migration to the sample near surface zone [18]) and the fluorite reduction (with concomitant Ce^{3+} creation). The elimination of Cu from the fluorite lattice is expected to produce an increase of the fluorite cell parameter (see the comparison of the Cu20Ce80 and CeO₂ references in Fig. 3) as it occurs also upon ceria reduction or thermal expansion [4,10,18]. In any case, we can note that the overall effect of the WGS reaction on the fluorite cell parameter is more drastic in the ternary W–Cu–Ce systems with respect to all binary parent Cu–Ce and, particularly, W–Ce materials. Moreover, the redox behavior of W–Ce materials evidences slower reduction kinetics: they are not able to achieve quasi-equilibrium states in conditions under which the ternary system does. The single technique XRD study is thus able to show that the fluorite phase of W–Cu–Ce materials becomes strongly reduced under WGS conditions to a comparatively higher extent than corresponding binary reference materials and with concomitant production of metallic Cu. Ce L_{III}-edge XAS data (see Fig. S2) agrees with this and show the presence of a significant number of oxygen vacancies at reaction conditions, evidenced by the corresponding decrease of the Ce–O first coordination number.

To quantify the response of the systems, we carried out a series of XRD and XAS isothermal experiments with the materials

subjected to the WGS atmosphere at 300 °C. Detailed analysis of the fluorite-type structure behavior was carried out first with XRD. Fig. 4 reports the results for the W10Cu20Ce70 (and corresponding W10Ce90 reference) case while others are presented in Fig. S3 (supporting information). The fluorite cell parameter suffers first the thermal expansion at 300 °C and displays thus increasing or decreasing successive behavior depending on the nature of the gas phase. First, under a reducing CO atmosphere, there is a large increase of the cell dimension/volume which is partially offset under the complete WGS mixture. Note that the result indicates a partially reduced state which can switch reversibly under a subsequent treatment in a simple CO mixture and get a final value close to the initial one under an oxidizing (either H₂O or O₂) gas atmosphere. The evolution of the cell parameter clearly points out to the redox nature of the catalyst behavior, as it was previously noted for the parent Cu20Ce80 sample [4]. The interaction with CO reduces the fluorite promoter phase while the corresponding interaction with H₂O re-oxidizes it. The result under the WGS mixture indicates the dominance of the reductive interaction in reaction conditions and thus the possible relevancy of ceria vacancies on the catalytic behavior, most particularly for oxidative steps. Of course, both CO and H₂O interactions must occur mainly at the metal-support interface while in any case the role of ceria oxygen vacancies becomes evident from the data [4]. More interestingly, the W–Ce reference

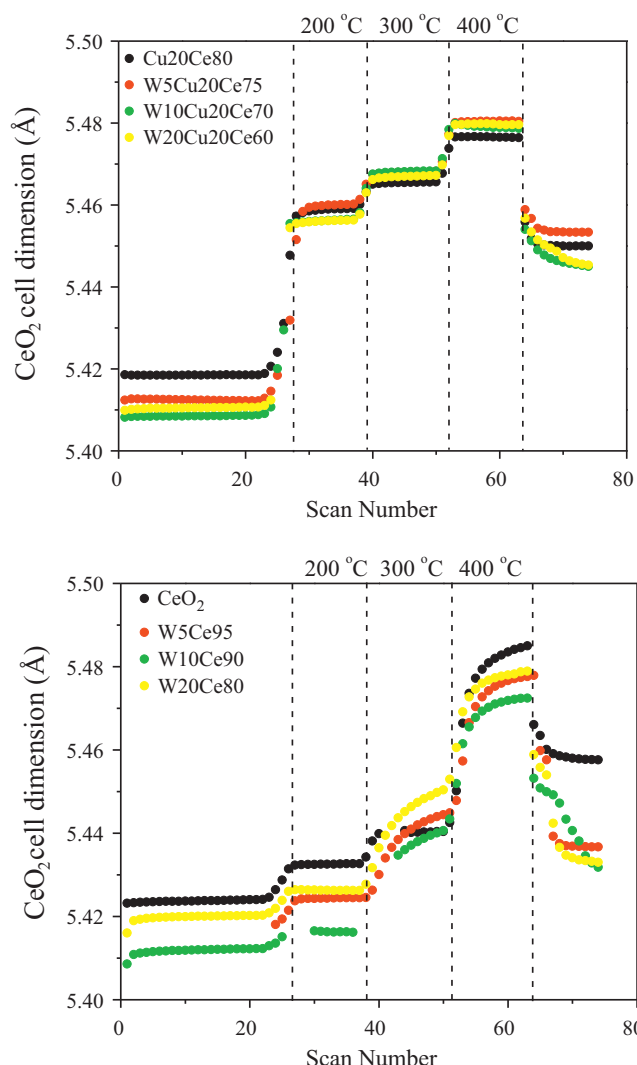


Fig. 3. Fluorite cell parameter observed for W–Cu–Ce and Cu–Ce, W–Ce and CeO₂ reference materials during the WGS temperature ramp and indicated isothermal steps (same as Fig. 2). Last step (not labeled) corresponding to cooling to RT.

system shows a relatively similar response although the extent of redox activity becomes severely damped indicating the need of Cu to trigger this behavior.

Additionally, we note that Cu maintains a fully reduced state according to XRD in all steps of Fig. 4 containing CO at the gas phase (CO/He, CO + H₂O/He). No changes are thus observed in this metallic phase in absence/presence of water. In all other steps Cu appears in a dominant oxidized state. This behavior exactly mimics the one previously reported for the parent Cu₂₀Ce₈₀ sample [4].

Full comparison of the fluorite lattice parameter redox behavior during the isothermal experiment among samples and references is given in Fig. 5. The fluorite cell parameter (given in Table S2 of the supporting information) is here normalized to 1 under He to (i) roughly get rid of thermal effects and (ii) facilitate a comparative analysis uncovering differential effects among samples. Worth to note is the trend observed in the parameter changes: W–Ce references display a redox behavior similar to the CeO₂ material, Cu–Ce suffers the strong redox changes already mentioned and, finally, the ternary systems show significantly larger ones. The binary Cu–Ce and W–Ce effects on fluorite reduction/oxidation may be qualitatively predicted due to the well known influence of Cu in the redox behavior of Ce [4,38,39] and the relatively small effect of W [40]. In order to completely interpret the W–Cu–Ce ternary

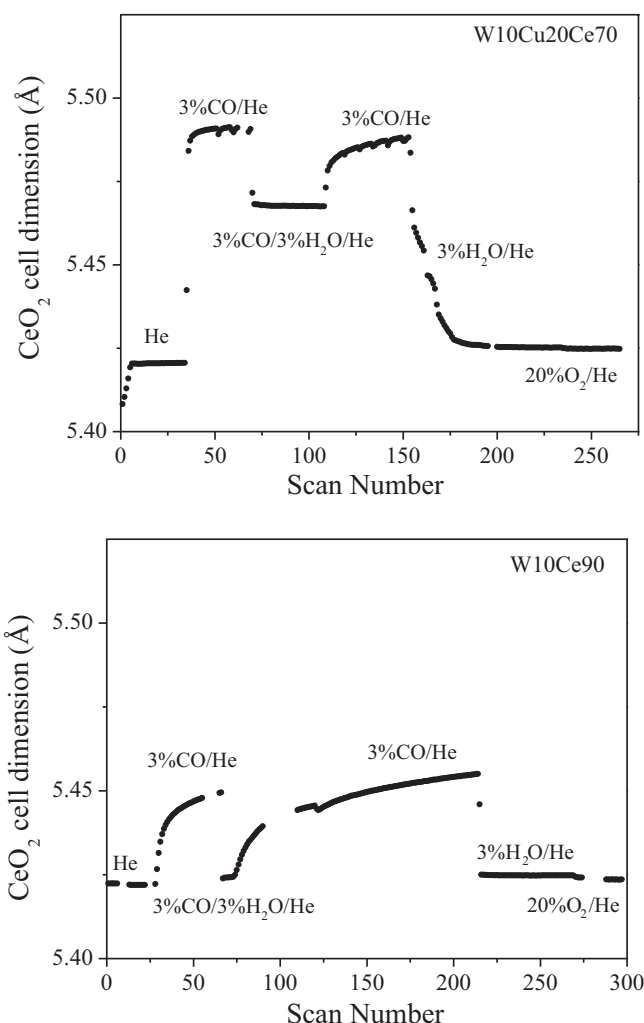


Fig. 4. Fluorite lattice parameter during an isothermal gas-switch experiment at 300 °C for W10Cu20Ce70 and W10Ce90 reference materials under indicated gas mixtures.

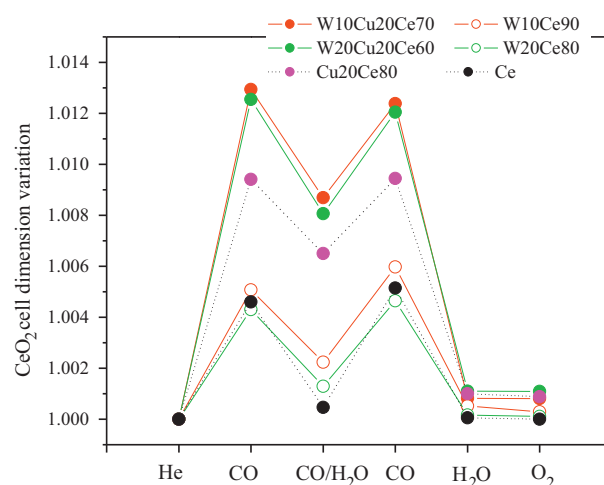


Fig. 5. Fluorite cell parameter variation during the isothermal gas-switch experiment at 300 °C illustrated in Fig. 4.

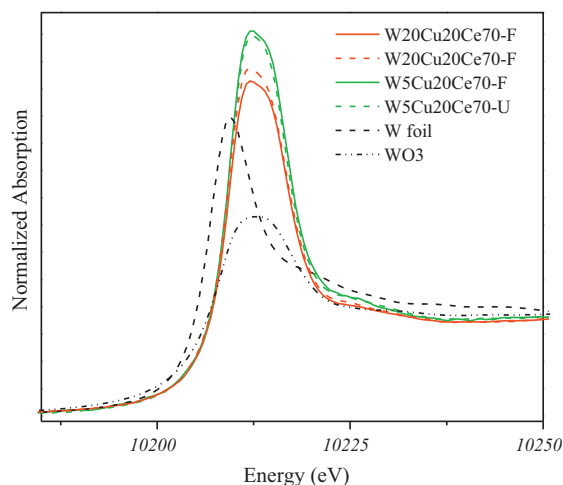


Fig. 6. W_{LIII}-edge XANES spectra for fresh and used (isothermal WGS at 300 °C) W–Cu–Ce and reference samples.

system behavior we carried out a XAS study of Cu and W state (presented below). In any case the absence of significant evolution in the Cu metallic phase between CO/He and CO + H₂O/He steps provides evidence of a W direct influence in fluorite redox properties through the managing of oxygen vacancies. A synergetic rather than additive effect (see comparison between binary W–Ce plus Cu–Ce reference and W–Cu–Ce ternary systems) applies thus to both the reduction (e.g. interaction with CO in the WGS mixture; Fig. 5) and “oxidation” (e.g. interaction with water in the WGS mixture; Fig. 5) of the fluorite phase. Worth to stress is that Fig. 5 displays values at quasi-equilibrium conditions reached in Figs. 4 and S3 at the different gas-phase steps, so the W influence on fluorite-structure-redox properties concerns primarily the number of oxygen vacancies (a thermodynamic property) but Figs. 4 and S3 also provide evidence of a fast kinetics for formation (reduction) and annihilation (oxidation) of such punctual defects.

A XAS study at the W_{LIII}- and Cu K-edges was devoted to analyzing the role of these two cations in the WGS reaction. Starting first with W, Fig. 6 displays XANES W_{LIII}-edge results. Figs. 7 and 8 additionally report, respectively, the Fourier Transform (module and imaginary part) of the EXAFS signals as well as some fitting results. The analysis of the XANES edge region (Fig. S4 of the supporting information presents the second derivative of the spectra) in Fig. 6 indicate the W⁶⁺ chemical state of the cation, irrespective of being

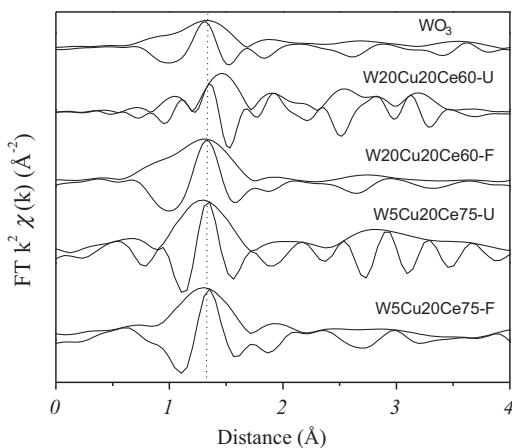


Fig. 7. Module and imaginary part of W_{LIII}-edge Fourier Transform EXAFS signals ($k = 2.58\text{--}11.15\text{ Å}^{-1}$ for all samples) for fresh and used (isothermal WGS at 300 °C) W–Cu–Ce and WO₃ reference samples.

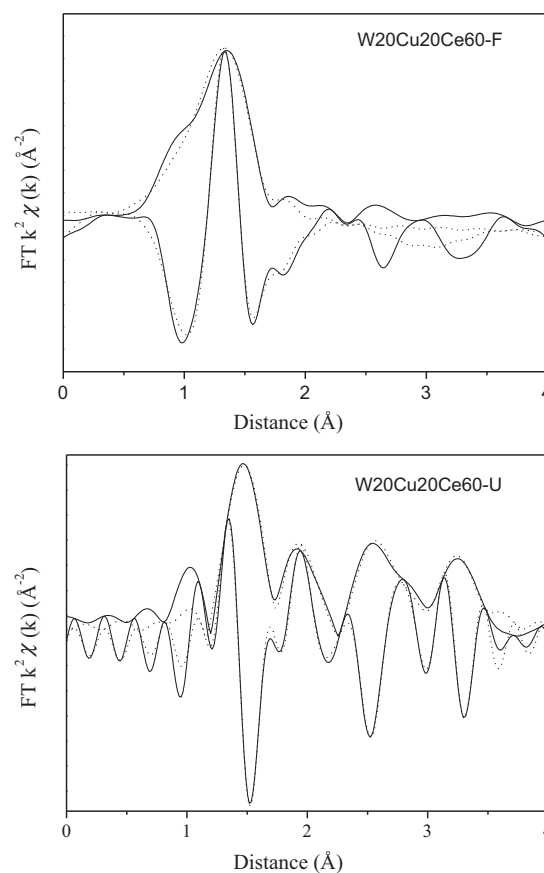


Fig. 8. Module and imaginary part of W_{LIII}-edge Fourier Transform EXAFS (solid line) and simulated (dashed line) signals for fresh and used (isothermal WGS at 300 °C) W20Cu20Ce60 sample.

at the initial state or after WGS reaction. The intensity of the white line (Fig. 6) as well as the d-states splitting (Fig. S3) indicates the tetrahedral environment of W, characterized by a large s-p/d re-hybridization and a relatively small d splitting [41]. Moreover, this is confirmed with the EXAFS analysis of the samples, which showed a coordination number of 4 for the fresh samples (Table 1). Differences with the single oxide (monoclinic) WO₃ reference obtained using the same preparation method are obvious in Figs. 6 and 7 and strongly suggest the inclusion of W into the dominant fluorite-type phase detected by XRD. A potential alternative could be the presence of an amorphous surface WO_x phase but this can be ruled out with the help of Raman (Fig. 9). W–O and W–O–W frequencies characteristic of surface WO_x entities at ca. 930 and 825 cm^{−1} are only detected in binary W–Ce materials [42]. So, W strongly distorts the fluorite environment and adopts a tetrahedral local coordination in all ternary W–Cu–Ce samples. This calls for a local environment similar to cerium tungstate (a T_d local symmetry for W [43]) but likely within a fluorite network. Unfortunately, Raman can not give a conclusive assignment as the most prominent band of such local arrangements would appear at about 920–950 cm^{−1} but our ceria-related samples showed the presence of additional strongly adsorbed oxygen species (957 cm^{−1} for peroxide and ca. 1150 cm^{−1} for superoxide species) or second-order fluorite bands at such range [44–46]. In any case, the combined XRD-XANES-EXAFS-Raman characterization clearly identifies the W chemical and structural characteristics as being part of a strongly distorted T_d type local environment not compatible with any crystallized or (surface-related) amorphous single WO_x phase.

Interestingly, the W cation suffers a strong reordering in the case of ternary samples with W content higher than that in

Table 1W_{LIII} EXAFS fitting results for the W₂₀Cu₂₀Ce₆₀ sample before (-F) and after (-U) WGS reaction at 300 °C.

| Shell | C.N. | R/Å | $\Delta\sigma^2/10^3 \times \text{\AA}^2$ | E_0/eV |
|---|------------------------|-------------|---|-----------------|
| W ₂₀ Cu ₂₀ Ce ₆₀ -F: 2.55–11.16 Å ⁻¹ ; 0.65–1.97 Å; 7 ^a | | | | |
| W–O | 3.7 ± 0.4 | 1.78 ± 0.01 | 0.66 ± 0.1 | 3.0 ± 1 |
| W ₂₀ Cu ₂₀ Ce ₆₀ -U: 2.58–12.60 Å ⁻¹ ; 0.82–3.65 Å; 18 ^a | | | | |
| W–O | 0.9 ₅ ± 0.1 | 1.81 ± 0.01 | 0.56 ± 0.1 | 6.1 ± 1 |
| W–O | 2.1 ± 0.3 | 2.43 ± 0.01 | 0.58 ± 0.09 | 4.1 ± 1 |
| W–O | 3.0 ± 0.4 | 2.86 ± 0.02 | 0.26 ± 0.12 | 8.1 ± 1.2 |
| W–Cu | 1.2 ± 0.3 | 3.54 ± 0.02 | 1.1 ± 0.13 | 7.4 ± 1.1 |

^a Sample name; *k* and *R* ranges of fitting and number of free parameters according to the Nyquist Theorem.

W₅Cu₂₀Ce₇₅. Thus, while the W environment in the later sample is more or less stable (Fig. 7), it suffers a strong reordering effect in the case of the W₂₀Cu₂₀Ce₆₀ sample. The EXAFS fitting (Table 1) gives W–O and W–Cu coordination distance pointing out to a structure resembling that of triclinic copper tungstate, CuWO₄ [47,48]. The W–Cu coordination number indicates rather small nuclei, far from the bulk number (7). Also, W–W contributions were not detected indicating that homo-atom contact is not produced in the material. The EXAFS result is fully confirmed by Raman; the inset of Fig. 9 displays the characteristic Raman lines of this compound [49], which were detected using Raman in W₁₀Cu₂₀Ce₇₀ and W₂₀Cu₂₀Ce₆₀ samples. It becomes thus evident that most active samples suffer an evolution at WGS reaction conditions not only involving Cu but also W. Tungsten seems to be stabilized in a local CuWO₄ type local arrangement in close contact with the fluorite-type structure and influencing its redox behavior.

The Cu K-edge was also investigated. Fig. 10 illustrates the copper evolution in WGS reaction conditions through the Fourier Transform of the corresponding EXAFS signals. Comparison with pertinent reference compounds evidences that, in accordance with XRD, such evolution goes from a fully oxidized Cu²⁺ state to a dominant metallic fcc one. Differences among samples are however evident while analyzing both XANES (Fig. S5 supporting information) or FT EXAFS data (Fig. 11) [50]. For W₅Cu₂₀Ce₇₅, both techniques show the presence of a minor Cu⁺ (Cu₂O-type) phase

with distinctive Cu–O and Cu–Cu distances at, respectively, 1.86 and 2.91 Å (Table 2) [36]. As such oxide phase was essentially XRD silent in the experiments carried out (Fig. 2), it would appear that it corresponds to a surface layer or patch decorating the metal Cu(0) fcc particles. Note that the EXAFS distances are incompatible with any Cu⁺ (and Cu²⁺) W–Cu mixed oxide phase [47,51]. As previously mentioned, the nanosized W–Cu entities appear to have a rather limited number of Cu atoms around W centers, constituting thus a small fraction of the copper (undetected by XANES and EXAFS, e.g. below 5–10 at.% of total content) and not having any apparent redox capability by itself (as Cu remains at a Cu²⁺ state in the W–Ce local environment during WGS up to 450 °C).

The copper oxide phase is not observed using XAS techniques (Figs. 11 and S5) for the other W–Cu–Ce samples as the single Cu–O contribution detected appears related to a metal-support contact. This could be compatible with a surface Cu₂O-like phase which relative importance decreases as copper particle size grows. According to the 1st and 2nd shell Cu–Cu metal C.N.s reported in Table 2, the metal particle grows from ca. 10 to 200 atoms in going from W₅Cu₂₀Ce₇₅ to W₂₀Cu₂₀Ce₆₀, with a dispersion decrease from ca. 1 to ca. 0.55 [52]. Assuming a similar thickness surface layer (or in other words a similar depth for the surface Cu “oxidation” of the metal particles) for all samples and considering the dispersion differences already discussed, the corresponding Cu₂O-type contribution should have been detected in all W–Cu–Ce materials.

To further analyze the importance of such copper-containing surface phase, an in situ IR study during WGS at variable temperature was carried out. Fig. 12 plots the C–O stretch region and provides evidence for presence of a band at 2105–2112 cm⁻¹, behaving similarly with temperature for all samples. The thermal stability and frequency are both characteristic of carbonyl species chemisorbed on Cu⁺ cations [4,53]. This species disappears at 300 °C due to a limited thermal stability of the adsorbed probe molecule (CO). Therefore, the combination of XRD (Fig. 2), XAS

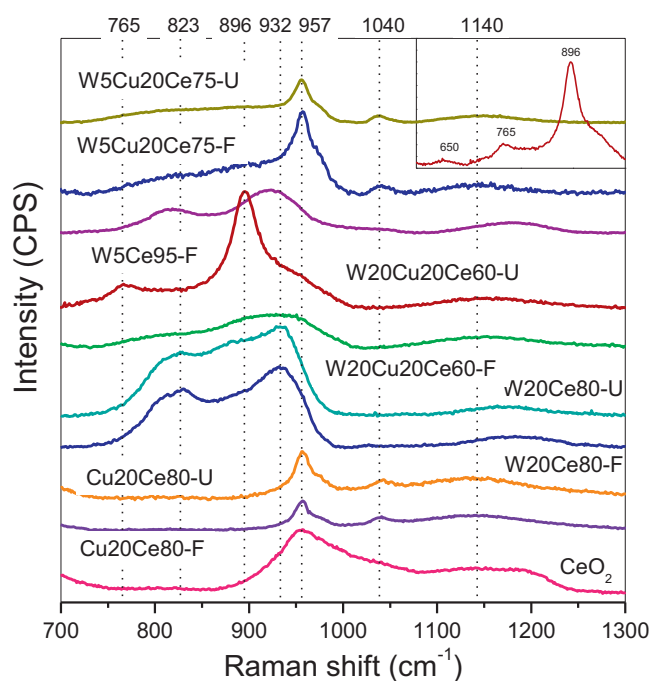


Fig. 9. Raman spectra for fresh and used (isothermal WGS at 300 °C) W–Cu–Ce and W–Cu, Cu–Ce and CeO₂ reference materials. The inset displays the frequency region with characteristic peaks of a CuWO₄ phase.

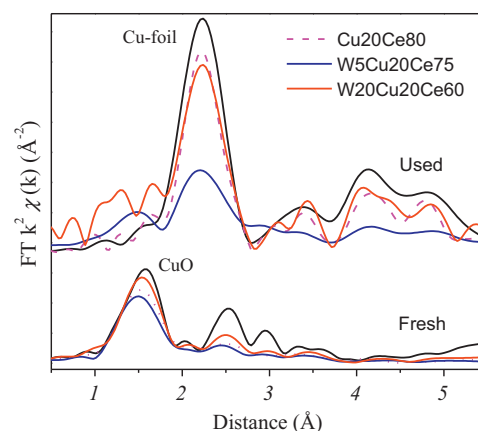


Fig. 10. Module and imaginary part of Cu K-edge Fourier Transform EXAFS signals ($k = 2.74$ – 11.40 \AA^{-1} for all samples) for fresh and used (isothermal WGS at 300 °C) W–Cu–Ce and Cu/CuO reference samples.

Table 2
Cu K EXAFS fitting results for W5Cu20Ce75 and W20Cu20Ce60 samples after WGS reaction at 300 °C.

| Shell ^b | C.N. | R/Å | $\Delta\sigma^2/10^3 \times \text{\AA}^2$ | E_0/eV |
|--|-------------|-------------|---|-----------------|
| W5Cu20Ce75-U: 3.05–12.47 Å ⁻¹ ; 0.98–3.64 Å; 16 ^a | | | | |
| Cu–O (ox) | 0.95 ± 0.02 | 1.86 ± 0.01 | 2.6 ± 0.2 | 5.4 ± 1 |
| Cu–Cu (m) | 2.7 ± 0.4 | 2.51 ± 0.02 | 0.67 ± 0.07 | 0.8 ± 1 |
| Cu–Cu (ox) | 0.9 ± 0.2 | 2.91 ± 0.02 | 0.70 ± 0.1 | −9.0 ± 1 |
| Cu–Cu (m) | 1.0 ± 0.2 | 3.52 ± 0.02 | 0.67 ± 0.07 | −4.1 ± 1 |
| W20Cu20Ce60-U: 2.74–12.77 Å ⁻¹ ; 0.98–3.67 Å; 17 ^a | | | | |
| Cu–O (m-supp) | 2.2 ± 0.3 | 1.76 ± 0.02 | 1.3 ± 0.2 | −10.1 ± 1.2 |
| Cu–Cu (m) | 8.9 ± 0.6 | 2.54 ± 0.01 | 0.87 ± 0.06 | 2.3 ± 1 |
| Cu–Cu (m) | 4.0 ± 0.3 | 3.60 ± 0.02 | 0.95 ± 0.05 | 8.1 ± 1 |

^a Sample name; k and R ranges of fitting and number of free parameters according to the Nyquist Theorem.

^b (ox) stands for a contribution characteristic for an oxidized Cu(I) phase; (m) for metallic Cu(0) fcc and (m-supp) for metal Cu(0) support (fluorite-phase) contributions.

(Figs. 10 and 11) and DRIFTS (Fig. 12) strongly suggests the presence of a Cu₂O-type surface layer or patches onto the Cu(0) particles, formed above 200 °C in all samples under WGS reaction conditions. However, such surface entities seem to be significant at or above 300 °C only for the W5Cu20Ce75 sample.

Thus, the presence of W also alters the copper phase behavior under reaction conditions. For W5Cu20Ce75 we observed two different phenomena with respect to the Cu20Ce80 reference; the stabilization of a Cu₂O-type surface layer and a decrease of the Cu metal particle size. These effects according to chemical activity (Figs. 1 and S1) have relatively neutral or slightly negative effects on activity. Both effects are however not observed in the other W–Cu–Ce samples which present a similar Cu(0) particle size (Fig. 10) and minimal copper-phase related differences with

respect to the Cu20Ce80 reference (Fig. 12). For a W content above 10 at.% we however observed W–Cu (CuWO₄-type) local entities likely acting as interface agents between the dominant metallic Cu and fluorite-type phases. This seems a unique environment directly linked with the activity boost (Fig. 1S and S1). A new interface W–Cu phase appears thus a unique feature of the system which enhances activity with respect to Cu–Ce materials.

A last point to discuss concerns the reaction mechanism. In situ DRIFT experiments for the W10Cu20Ce70 sample are presented in Fig. 13 as a representative example of the surface species detected at reaction conditions. This plot can be compared with previous result for the Cu20Ce80 reference [4]. Fig. 13 shows, in addition of CO-carbonyls presented in Fig. 12, the formation of carbonates (region below 1750 cm⁻¹) and hydroxyls (above 3000 cm⁻¹) at or below 250 °C. Bidentate carbonates or carboxylates (bands at ca. 1530, 1345 cm⁻¹ [4,15,54]) were formed and seem reversible removed from the surface in absence of CO with concomitant decrease in CO₂ production. At higher temperatures, peaks associated with formates (ca. 2925, 2845, 1595, 1380 cm⁻¹) and monodentate carbonates (ca. 1460, 1390, 1370 cm⁻¹) were detected [4,15,54]. Presence of Ce³⁺ is also evidenced by a broad bump at ca. 2000 cm⁻¹. The high-temperature adsorbed species are strongly held at the surface (e.g., no intensity variation in absence of CO) and are likely spectators with little importance in the reaction mechanism. This is in agreement with current knowledge about the low importance of formate and, possibly, carboxylate species as key intermediates for highly active WGS systems [4,15].

The XRD/XAS/DRIFTS results are in agreement with a redox-type reaction mechanism by which CO adsorbs at the metal sites and then reacts with ceria at the interface to form CO₂ and

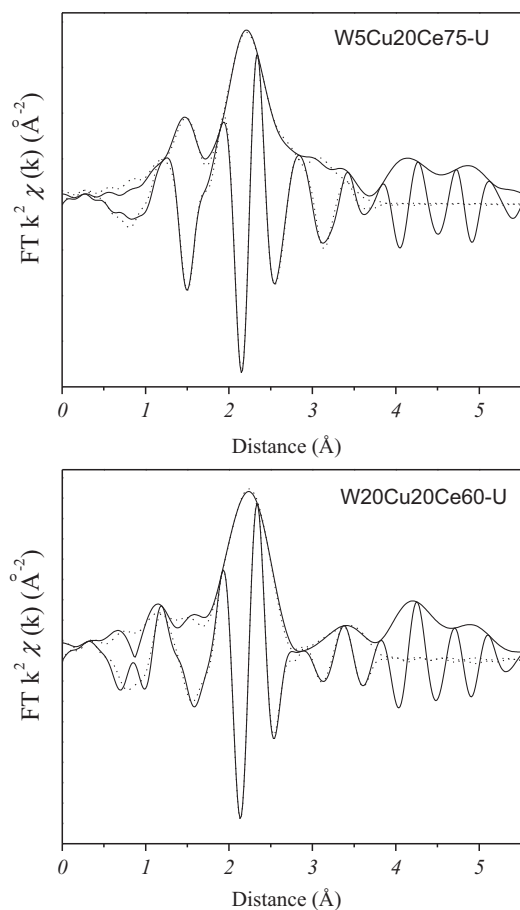


Fig. 11. Module and imaginary part of Cu K-edge Fourier Transform EXAFS (solid line) and simulated (dotted lines) signals for fresh and used (isothermal WGS at 300 °C) W–Cu–Ce samples.

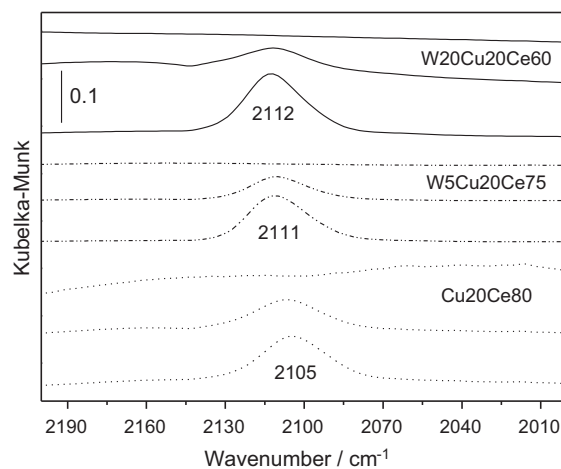


Fig. 12. DRIFT spectra of W–Cu–Ce and Cu–Ce reference materials under WGS atmosphere at 200, 250 and 300 °C (from bottom to top within each series). Cu20Ce80: dotted lines; W5Cu20Ce75; dash-dotted lines; W20Cu20Ce60: solid lines.

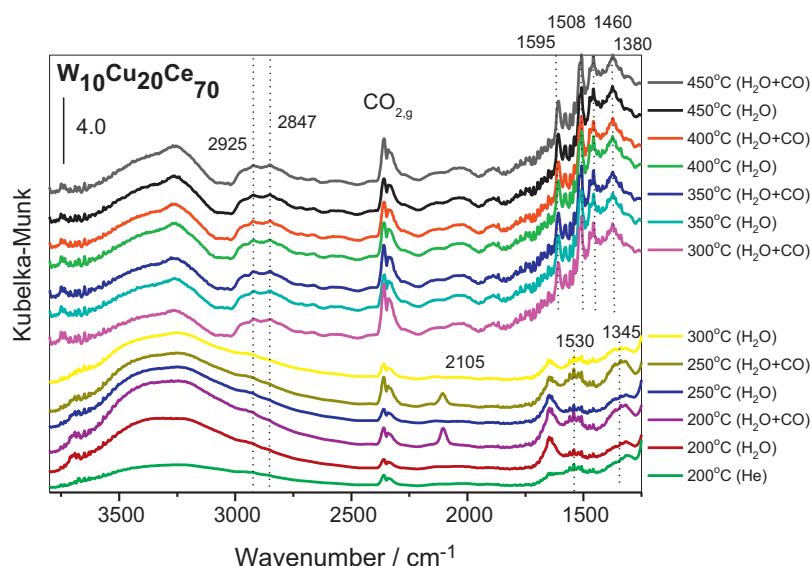


Fig. 13. In situ DRIFTS experiments recorded during isothermal treatment in presence of water or the WGS reaction mixture for the W10Cu20Ce70 sample. See text for details.

oxygen vacancies. The water undergoes decomposition near such vacancies, filling them with concomitant generation of H_2 and completion of the catalytic cycle [2,4,15,54,55]. Fig. 13 may suggest that bidentate carbonates can be intermediates in the CO activation as are reversibly formed at low temperatures in presence/absence of CO. However, strong evidence of a carbonate-related deactivating effect in the WGS reaction due to a blocking effect at the Cu–CeO₂ interface has been accumulated in recent reports [4,54,56]. This would thus suggest that to form CO₂, CO reacts directly at the metal-promoter interface without forming carboxylate-type species. Such point requires however further experiments to be definitively settled down.

4. Conclusions

A series of ternary W–Cu–Ce mixed oxide systems prepared by microemulsion display excellent catalytic performance for the production of hydrogen through the WGS. At low temperatures (<350 °C), the total conversion of CO on the W–Cu–Ce systems was two times larger than on binary Cu–Ce mixed oxides which are well known catalysts for the WGS. In addition, when compared to Cu–Ce and Cu–Zn catalysts, the W–Cu–Ce catalysts appeared quite stable and no signs of deactivation were found after 10 h of reaction time. The catalyst properties were evaluated and interpreted on the basis of a XRD–XAS–Raman–DRIFTS multitechnique approach. The solids were analyzed in terms of their long and short range order and redox behavior and key physico-chemical parameters were identified to interpret catalytic properties on a physical basis.

The multitechnique scrutiny of the samples provides conclusive evidence that W can modify all chemical phases present during the WGS reaction. At WGS reaction conditions and as previously shown in the parent Cu–Ce mixed oxide, the study carried out detected the dominant presence of metallic Cu and fluorite-type phases. In the W–Cu–Ce ternary systems displaying high activity (e.g. W content above 10 at.%) we additionally detected the presence of oxidized W–Cu local entities. In the presence of such entities, both the fluorite reduction by interaction with CO at metal-promoter interfaces and its oxidation by interaction with H₂O are strongly promoted, evidencing an overall improvement of the ceria redox capabilities with a concomitant effect in WGS activity. The presence of such W–Cu entities leads to highly active and stable WGS catalysts (for

W contents above 10 at.% in the initial mixed oxide) being thus of practical importance in the low temperature region, where useful systems are actively sought.

Acknowledgements

A.K. would like to thank the Ramón y Cajal Project of MICINN (Spain) for a Postdoctoral Fellowship. P.M. wants to acknowledge EU (Project no. UDA-POKL.04.01.01-00-029/10-00) for financial support of a stay at Madrid (ICP-CSIC). The work performed at BNL was supported by the U.S. Department of Energy, Office of Basic Energy Sciences, Chemical Science Division (DE-AC02-98CH10886). The NSLS is supported by the Chemical and Materials Science Divisions of the U.S. Department of Energy. Financial support by Spanish “Plan Nacional” Projects CTQ2010-14872 and CTQ2009-14527 and by the Comunidad de Madrid (Project DIVERCEL, Ref.: S2009/ENE-1475) is acknowledged.

Appendix A. Supplementary data

Supplementary data associated with this article can be found, in the online version, at <http://dx.doi.org/10.1016/j.apcatb.2012.12.013>.

References

- [1] G.E.H. Knozinger, J. Weitkamp (Eds.), *Handbook of Heterogeneous Catalysis*, VCH, Berlin, 1997.
- [2] C. Ratnasamy, J.P. Wagner, *Catalysis Reviews* 51 (2009) 325.
- [3] A. Trovarelli (Ed.), *Catalysis by Ceria and Related Materials*, World Scientific, London, 2002.
- [4] X. Wang, J.A. Rodriguez, J.C. Hanson, D. Gamarra, A. Martínez-Arias, M. Fernández-García, *Journal of Physical Chemistry B* 110 (2006) 428.
- [5] L. Szabova, M.F. Camellone, M. Huang, V. Matolin, S. Fabris, *Journal of Chemical Physics* 133 (2010) 234705.
- [6] R. Si, J. Raitano, N. Yi, L. Zhang, S.-W. Chan, M. Flytzani-Stephanopoulos, *Catalysis Today* 180 (2012) 68.
- [7] M. Fernández-García, A. Martínez-Arias, J.C. Hanson, J.A. Rodriguez, *Chemical Reviews* 104 (2004) 4063.
- [8] (a) W. Liu, M. Flytzani-Stephanopoulos, *Journal of Catalysis* 153 (1995) 304; (b) W. Liu, M. Flytzani-Stephanopoulos, *Journal of Catalysis* 153 (1995) 317; (c) Y. Li, Q. Fu, M. Flytzani-Stephanopoulos, *Applied Catalysis B* 27 (2000) 179; (d) X. Qi, M. Flytzani-Stephanopoulos, *Industrial & Engineering Chemistry Research* 43 (2004) 3055; (e) Y. Li, Q. Fu, M. Flytzani-Stephanopoulos, *Catalysis Today* 93/95 (2004) 241.

- [9] (a) S. Park, J.M. Vohs, R.J. Gorte, *Nature* 404 (2000) 265;
(b) R.J. Gorte, J.M. Vohs, S. McIntosh, *Solid State Ionics* 175 (2004) 1;
(c) G. Zhou, J.C. Hanson, R. Gorte, *Applied Catalysis A: General* 335 (2008) 153.
- [10] (a) J.A. Rodríguez, J.C. Hanson, J.-Y. Kim, G. Liu, A. Iglesias-Juez, M. Fernández-García, *Journal of Physical Chemistry B* 117 (2003) 3535;
(b) J.A. Rodríguez, J.C. Hanson, J.-Y. Kim, G. Liu, A. Iglesias-Juez, M. Fernández-García, *Journal of Chemical Physics* 119 (2003) 5659;
(c) X. Wang, J.C. Hanson, G. Liu, J.A. Rodríguez, A. Iglesias-Juez, M. Fernández-García, *Journal of Chemical Physics* 121 (2004) 5434;
(d) X. Wang, J.C. Hanson, J.A. Rodríguez, C. Belver, M. Fernández-García, *Journal of Chemical Physics* 122 (2005) 154711;
(e) M. Fernández-García, X. Wang, C. Belver, A. Iglesias-Juez, J.C. Hanson, J.A. Rodríguez, *Chemistry of Materials* 17 (2005) 4181.
- [11] (a) B.M. Reddy, P. Saika, P. Bharali, Y. Yamada, T. Kobayashi, M. Mohler, W. Grunet, *Journal of Physical Chemistry C* 112 (2008) 16393;
(b) B.M. Reddy, G. Thirumuthulu, L. Katta, Y. Yamada, S.E. Park, *Journal of Physical Chemistry C* 113 (2009) 15882;
(c) B.M. Reddy, L. Katta, G. Thirumuthulu, *Chemistry of Materials* 22 (2010) 467.
- [12] (a) W. Mista, M.A. Malecka, L. Kepinski, *Applied Catalysis A* 368 (2009) 71;
(b) M. Kurnatowska, L. Kepinski, W. Mista, *Applied Catalysis B* 117/118 (2012) 135.
- [13] (a) J.B. Park, J. Graciani, J. Evans, D. Stacchiola, S. Ma, P. Liu, A. Nambu, J.F. Sanz, J.F.J. Hrbek, J.A. Rodríguez, *Proceedings of the National Academy of Sciences of the United States of America* 106 (2009) 4975;
(b) J. Graciani, J.J. Plata, J.F. Sanz, P. Liu, J.A. Rodríguez, *Journal of Chemical Physics* 132 (2010) 104703.
- [14] (a) J.Q. Wang, M.Q. Shen, Y. An, J. Wang, *Journal of Catalysis Communications* 10 (2008) 103;
(b) A.D. Mayernick, M.J. Janik, *Journal of Physical Chemistry C* 112 (2008) 14955;
(c) M. Jobaggy, C. Sorbello, E.E. Eliseo, *Journal of Physical Chemistry C* 113 (2009) 10853;
(d) S. Watanabe, X.L. Ma, C.S. Song, *Journal of Physical Chemistry C* 113 (2009) 14249;
(e) L.S. Liu, B. Liu, D.L. Dong, J. Zhu, H.Q. Wang, K.Q. Sun, B. Zhao, H.Y. Zhu, L. Dong, Y. Chen, *Applied Catalysis B* 90 (2009) 578;
(f) X.B. Chen, G.S. Li, Y.G. Su, X.Q. Qui, L.P. Li, Z.G. Zhou, *Nanotechnology* 20 (2009) 115606;
(g) H.F. Wang, X.Q. Gong, Y.L. Gou, G.Z. Lu, P. Hu, *Journal of Physical Chemistry C* 113 (2009) 10229;
(h) G.R. Li, D.L. Qu, Z.L. Wang, C.J. Su, Y.X. Tong, L. Arault, *Chemical Communications* (2009) 7557;
(i) U.S. Ozkan, H. Song, *Journal of Physical Chemistry A* 114 (2010) 3796;
(j) C. Chatzichitodoulou, P.V. Hendriken, A.M. Hagen, *Journal of the Electrochemical Society* 157 (2010) 3299;
(k) M. Guo, J. Lu, Q. Bi, M. Luo, *ChemPhysChem* 11 (2010) 1699;
(l) J. Li, P. Zhu, R. Zhou, *Journal of Power Sources* 196 (2011) 9590;
(m) J.A. Sullivan, P. Dulgheru, I. Atriback, A. Bueno-López, A. García-García, *Applied Catalysis B* 108/109 (2011) 134.
- [15] R. Burch, A. Goguet, F.C. Meunier, *Applied Catalysis A* 409/410 (2011) 3.
- [16] C. Kalamaras, S. Americanou, A.M. Efstathiou, *Journal of Catalysis* 279 (2011) 287.
- [17] F. Yang, Y.M. Choi, S. Agnoli, P. Liu, D. Stacchiola, J. Hrbek, J.A. Rodríguez, *Journal of Physical Chemistry C* 115 (2011) 23062.
- [18] X. Wang, J.A. Rodríguez, J.C. Hanson, D. Gamarra, A. Martínez-Arias, M. Fernández-García, *Journal of Physical Chemistry B* 109 (2005) 19595.
- [19] J. Ciston, J.A. Rodríguez, J.C. Hanson, A. Martínez-Arias, M. Fernández-García, Y. Zhu, *Journal of Physical Chemistry C* 115 (2011) 13851.
- [20] M. Hatanaka, N. Takahashi, T. Tanabe, Y. Nagai, A. Suda, H. Shinjoh, *Journal of Catalysis* 266 (2009) 182.
- [21] T. Tabakova, V. Idrakev, J. Papavasiliou, G. Avgouropoulos, T. Ioannides, *Catalysis Communications* 8 (2007) 101.
- [22] D. Gamarra, B. Belver, M. Fernandez-García, A. Martinez-Arias, *Journal of the American Chemical Society* 129 (2007) 12064.
- [23] P.J. Chupas, X.Y. Qiu, J.C. Hanson, P.L. Lee, C.P. Grey, S.J.L. Billinge, *Journal of Applied Crystallography* 36 (2003) 1342.
- [24] M. Estrella, L. Barrio, G. Zhou, X.Q. Wang, Q. Wang, W. Wen, J.C. Hanson, A.I. Frenkel, J.A. Rodríguez, *Journal of Physical Chemistry C* 113 (2009) 14411.
- [25] A.P. Hammersley, S.O. Svensson, A. Thompson, *Nuclear Instruments & Methods A* 346 (1994) 312.
- [26] A.C. Larson, R.B.V.D. Los, *Alamos National Laboratory Report LAUR*, 2000, 86.
- [27] B.H. Toby, *Journal of Applied Crystallography* 34 (2001) 210.
- [28] M. Newville, B. Ravel, D. Haskel, J.J. Rehr, E.A. Stern, Y. Yacoby, *Physica B: Condensed Matter* 208 (1995) 154.
- [29] B. Ravel, M. Newville, *Journal of Synchrotron Radiation* 12 (2005) 537.
- [30] K.V. Klementev, *Journal of Physics D: Applied Physics* 34 (2001) 209.
- [31] J.J. Rehr, J.J. Kas, F.D. Vila, M.P. Prange, K. Jorissens, *Physical Chemistry Chemical Physics* 12 (2010) 5503.
- [32] L. Barrio, M. Estrella, G. Zhou, W. Wen, J.C. Hanson, A.B. Hungria, A. Hornés, M. Fernández-García, A. Martínez-Arias, J.A. Rodríguez, *Journal of Physical Chemistry C* 114 (2010) 3580.
- [33] P. Djinojic, J. Batista, J. Levec, A. Pintar, *Applied Catalysis A* 364 (2009) 156.
- [34] G. Germany, Y. Schuurman, *AIChE Journal* 52 (2006) 1806.
- [35] JCPDS Powder diffraction file: PDF No. 75-0151; International Center for diffraction data; Swthmore, Pa, (2010).
- [36] JCPDS Powder diffraction file: PDF No. 34-1354; International Center for diffraction data; Swthmore, Pa, (2010).
- [37] JCPDS Powder diffraction file: PDF No. 72-0629; International Center for diffraction data; Swthmore, Pa, (2010).
- [38] A.B. Kehoe, D.O. Scanlon, G.W. Watson, *Chemistry of Mater* 23 (2011) 4464.
- [39] N. Qiu, J. Zhang, Z. Wu, T. Hu, P. Liu, *Crystal Growth & Design* 12 (2012) 629.
- [40] Z. Hu, H. Metiu, *Journal of Physical Chemistry C* 115 (2011) 17898.
- [41] (a) S. Yamazoe, Y. Hitomi, T.S. Shishido, T. Tanaka, *Journal of Physical Chemistry C* 112 (2008) 6869;
(b) H. Asakura, T.S. Shishido, S. Yamazoe, K. Teramura, T. Tanaka, *Journal of Physical Chemistry C* 115 (2011) 23653.
- [42] (a) F.D. Hardcastle, I.E. Wachs, *Journal of Raman Spectroscopy* 26 (1995) 397;
(b) A. Fuerte, M.D. Hernández-Alonso, A.J. Maira, A. Martínez-Arias, M. Fernández-García, J.C. Conesa, J. Soria, G. Munuera, *Journal of Catalysis* 212 (2002) 1;
(c) L. Xiaowei, S. Mingmin, C. Yu, *Journal of Physical Chemistry C* 109 (2005) 3949.
- [43] (a) T. Gresling, H. Muller-Baschbaum, *Zeitschrift Fur Naturforschung Section B* 50 (1995) 1513;
(b) A.-S. Mamede, E. Payen, P. Grange, G. Poncelet, A. Ion, M. Alifanti, V.I. Parvulescu, *Journal of Catalysis* 223 (2004) 1.
- [44] R.Q. Long, Y.P. Huang, *Journal of Raman Spectroscopy* 28 (1997) 29.
- [45] The region of ca. around 1100–1300 cm⁻¹ has also contributions from weak second order longitudinal phonon modes, typical of nanosized materials. These are shown as broad bumps in our samples (see particularly the CeO₂ spectrum). For a complete discussion of these Raman modes see J.E. Spanier, R.D. Robinson, F. Zhang, S.-W. Chang, I.P. Herman, *Physical Reviews B* 64 (2001) 2454071.
- [46] W.H. Weber, K.C. Hass, J.R. Mc Bride, *Physical Review B* 48 (1993) 178.
- [47] JCPDS Powder diffraction file: PDF No. 72-0616; International Center for diffraction data; Swthmore, Pa, (2010).
- [48] O.Y. Khyzhun, V.C. Bekevar, Y.M. Solomin, *Journal of Alloys and Compounds* 48 (2009) 184.
- [49] J. Ruiz-Fuertes, M.N. Sanz-Ortiz, J. González, F. Rodríguez, A. Segura, D. Errandonea, *Journal of Physics Conference Series* 215 (2010) 012048.
- [50] Table 2 number of free parameters indicates that a maximum of 4 shells can be fitted in order to obtain EXAFS parameters values and errors. This only allows extracting information about the two first Cu metal coordination shells. Such limitation does not however have practical effects in terms of the accurate description the metal particle size using the 1st and 2nd shells coordination information.
- [51] JCPDS Powder diffraction file: PDF Nos. 78-0928; 80-1918; 84-1663. International Center for diffraction data; Swthmore, Pa, (2010).
- [52] (a) P. Menacherry, M. Fernández-García, G.L. Haller, *Journal of Catalysis* 166 (1997) 75;
(b) A. Jentys, *Physical Chemistry Chemical Physics* 1 (1999) 4059;
(c) G. Agostini, R. Pellegrini, G. Leofanti, L. Birtinetti, S. Bertarione, E. Groppo, A. Zecchina, C. Lamberti, *Journal of Physical Chemistry C* 113 (2009) 10485.
- [53] (a) A. Martínez-Arias, M. Fernández-García, J. Soria, J.C. Conesa, *Journal of Catalysis* 182 (1999) 367;
(b) P. Bera, A. López Cámara, A. Hornés, A. Martínez-Arias, *Journal of Physical Chemistry C* 113 (2009) 10689.
- [54] D. Gamarra, M. Fernández-García, C. Belver, A. Martínez-Arias, *Journal of Physical Chemistry C* 114 (2010) 18576.
- [55] Z. Yang, L. Xie, D. Ma, G. Wang, *Journal of Physical Chemistry C* 115 (2011) 673.
- [56] W. Deng, M. Flytzani-Stephanopoulos, *Angewandte Chemie International Edition* 45 (2006) 2285.